Journal of Magnetism and Magnetic Materials 595 (2024) 171611

Contents lists available at ScienceDirect

Journal of Magnetism and Magnetic Materials

journal homepage: www.elsevier.com/locate/jmmm

Research article

ESR and magnetization studies of double perovskite Sr_2FeNbO_6

D.V. Popov [a], R.G. Batulin [b], M.A. Cherosov [b], I.V. Yatsyk [a], T.I. Chupakhina [c], Yu.A. Deeva [c], R.M. Eremina [a,*], T. Maiti [d]

[a] Zavoisky Physical-Technical Institute, Federal Research Center "Kazan Scientific Center of RAS", Sibirsky tract, 10/7, 420029 Kazan, Russia
[b] Kazan (Volga Region) Federal University, Kremlevskaya st., 18, 420008 Kazan, Russia
[c] Institute of Solid State Chemistry of the Russian Academy of Sciences (UB), Pervomaiskaya St., 91, Yekaterinburg, 620990, Russia
[d] Department of Materials Science and Engineering, Indian Institute of Technology, Kanpur, 208016, India

ARTICLE INFO

Keywords:
ESR
Quasi one-dimensional system
Double perovskite
Curie–Weiss temperature

ABSTRACT

By pyrolysis of nitrate-organic mixtures, we synthesized double perovskite $Sr_2Fe_{0.6}NbO_{5.4}$. We performed the study of the temperature dependencies of the EPR spectra, DC and AC magnetization, and magnetization isotherms in a wide temperature range of 4–300 K. The EPR spectrum is described by the sum of two contributions below 125 K and indicates phase separation of the sample. The paramagnetic part of the inverse magnetic susceptibility is well approximated by the Curie–Weiss law with $\Theta_{CW} \approx -60$ K. The exchange integrals between iron spins, calculated from the temperature dependence of the ESR integral intensity and the Curie–Weiss temperature, coincide and are equal to $J/k_B \approx 10$ K. The negative sign of the Curie–Weiss temperature and the hysteresis loops indicate the antiferromagnetic canted nature of exchange interactions, which is further confirmed by the presence of a peak in the real part of the AC magnetization and its absence in the imaginary part.

1. Introduction

Double perovskites are being actively studied due to their extensive applications and wide variety of their physical properties. For example, double perovskite Sr_2FeNbO_6 is an efficient photocatalyst. When doped with Ti^{+4} with an optimal composition of $x = 0.07$, it generates a 1.5 times higher photocurrent and shows an enhanced quantum yield for the photodecomposition of methanol–water mixture [1].

A wide variety of techniques are used to synthesize double perovskites, so unambiguous crystal lattice parameters cannot be found in the literature. The Fm-3 m structure of the Sr_2FeNbO_6 samples with unit-cell lattice parameters $a = 7.8756$ Å and $c = 7.9375$ Å was obtained in [2]. As shown in [3], the Sr_2FeNbO_6 compound can have a cubic, tetragonal, or orthorhombic structure. According to DOS calculations, the tetragonal (I4/m) and orthorhombic (Pnma) crystal structures with the A-type AFM configuration serve as adequate models of the ground state [3]. The perovskite Sr_2FeNbO_6 has been shown to have a tetragonal structure with space group I4/m (87) and lattice parameters $a = 5.6078(1)$ Å and $c = 7.9658(1)$ Å [4]. The Sr_2FeNbO_6 ceramic was synthesized by a solid-state reaction of a stoichiometric mixture in [5]. X-ray diffraction patterns showed a single-phase perovskite with $a = 3.987(1)$ Å. The Sr_2FeNbO_6 ceramic was crystallized in a tetragonal unit cell with $a \approx b \approx 5.6$ Å and $c \approx 7.9$ Å [6]. The application of pressure induces a more rapid change in the parameter a than the parameter c, which indicates an increase in the magnitude of the octahedral tilting distortion [6]. According to [7], the Sr_2FeNbO_6 ceramic had an orthorhombic unit cell with Pbnm space group and lattice parameters $a = c = 5.60$ Å and $b = 7.96$ Å.

Different space groups and lattice parameters lead to conflicting data on the magnetic properties of Sr_2FeNbO_6. In [5], Sr_2FeNbO_6 was shown to exhibit a spin-glass transition at $T_G = 32.5$ K. However, in [7] it was established that Sr_2FeNbO_6 features a transition temperature of 20 K, again in a spin-glass state. In [8], it was shown that the Néel temperature of Sr_2FeNbO_6 is about 35 K. The provided values of phase transition temperatures differ greatly below the ordering temperature for $SrFeO_3$ which has a cubic structure with $a = 3.85$ Å and an antiferromagnetic transition at $T_N = 134$ K [9]. $SrNbO_3$ has the same perovskite-type structure but with a heavier transition metal Nb and a $4d^1$ electronic configuration of niobium and therefore exhibits metallic behavior. Bulk $SrNbO_3$ is not stable under ambient conditions [10].

The purpose of this work is to study the magnetic properties of Sr_2FeNbO_6 ceramics in the temperature range of 4–300 K via the magnetometry method and the electron-spin-resonance (ESR) data analysis.

2. Experimental results

Double perovskite $Sr_2Fe_xNbO_{6-\delta}$ was obtained by pyrolysis of nitrate-organic mixtures of the corresponding components. The details of the synthesis are presented in [11].

* Corresponding author.
E-mail address: REremina@yandex.ru (R.M. Eremina).

https://doi.org/10.1016/j.jmmm.2023.171611
Received 23 August 2023; Received in revised form 24 November 2023; Accepted 7 December 2023
Available online 10 December 2023
0304-8853/© 2023 Elsevier B.V. All rights reserved.

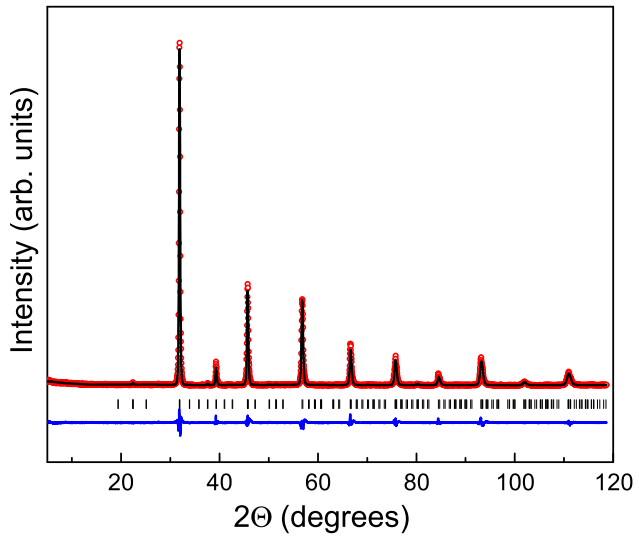

Fig. 1. X-ray diffraction pattern of Sr_2FeNbO_6: experiment (red squares) and its best fit (black line). Also shown is the difference between the experimental pattern and its best fit.

X-ray phase analysis (XFA) using the crystallographic database "Powder Standards Database PDF2" (ICDD, USA, Release 2009) showed that the sample is single-phase and contains a small number of impurities. The X-ray diffraction measurements of $Sr_2FeNbO_{6-\delta}$ were performed using the Shimadzu XRD-7000 S automatic diffractometer with a 2Θ range of 5–100° and a step of 0.02°. X-ray pattern processing was performed with the FULLPROF-2021 software. As was shown in our previous study [11], there are two ways to describe the $Sr_2Fe_xNbO_{6-\delta}$ diffraction pattern. The diffraction pattern and its fit by the Pbnm space group and lattice parameters $a = b = 5.605(7)$ Å, $c = 7.929(4)$ Å, and $V = 250.28(2)$ Å^3 are shown in Fig. 1.

XFA measurements performed via the Bruker S2 Ranger X-ray fluorescence spectrometer allowed us to determine ion concentrations where the ratios of the elements are Fe:Sr:Nb=0.17:0.55:0.28. Considering the electrical neutrality of the sample and the valences Fe^{3+}, Sr^{2+}, and Nb^{5+}, we calculated the oxygen content as 5.4. The actual formula of the sample is $Sr_2Nb_1Fe_{0.6}O_{5.4}$.

AC and DC magnetization measurements of the Sr_2FeNbO_6 compound were performed using the PPMS-9 device. DC magnetization was measured in zero-field cooling (ZFC) and field-cooling (FC) regimes at 100, 1000, and 10000 Oe and a temperature range of 5–300 K. The temperature dependencies of magnetization per unit magnetic field are shown in Fig. 2. The ZFC and FC curves begin to diverge below 40 K. The temperature dependencies of magnetization pass through a maximum in the 13–29 K range at 100 Oe and 1000 Oe typical for low-dimensional magnetic materials. It should be noted that the value of the magnetic susceptibility M/H is quite small. According to [12], the diamagnetism of a molecule can be determined in an additive fashion using the diamagnetic susceptibility of each ion. For $Sr_2FeNbO_{5.4}$, our calculations suggest $\chi_{DI} = 117.8 \cdot 10^{-6}$ emu/mol, which explains the discrepancy in the values of high-temperature magnetic susceptibility at different magnetic fields.

AC magnetization was measured at an external magnetic field of 10 Oe and frequencies of 10, 100, 1000, and 10000 Hz. The real and imaginary parts of AC magnetization are shown in Fig. 3. Magnetic field dependence of magnetization was measured for the Sr_2FeNbO_6 compound at external magnetic fields between −9 and 9 T and at temperatures of 5, 10, 20, 50, and 300 K.

EPR measurements were performed using a Bruker EMXPlus (X-band) and Bruker Elexsys E580-CW (Q-band) spectrometers, equipped with continuous-flow He and N_2 cryostats . In these measurements we used the X-band with a frequency of 9.4 GHz, a temperature range of 5–340 K, and Q-band with a frequency of 33.9 GHz, a temperature range of 10–40 K, and a magnetic-field range of 0–1.4 T. The ESR spectra are shown in Fig. 5.

Table 1
The Curie constant, the Curie–Weiss temperature, and the effective magnetic moments of Sr_2FeNbO_6.

H (Oe)	T_N (K)	T_{Ph} (K)	Θ_{CW} (K)	C (K emu/mol)	μ_{eff} (μ_B)	μ_{theor} (μ_B)
100			−60	1.87	3.86	
1000	14	25	−60	2.1	4.1	4.25
10000			−58	2	4	

3. Discussion

The temperature dependencies of the inverse magnetic susceptibility are shown in Fig. 2. The paramagnetic part of the inverse DC magnetization was approximated using the Curie–Weiss law (Fig. 2):

$$\chi = \frac{C}{T - \Theta_{CW}}. \quad (1)$$

The extracted Curie–Weiss temperature and Curie constant are given in Table 1. We also determined the experimental and theoretical effective magnetic moments of Sr_2FeNbO_6. The experimental magnetic moments were obtained using the Curie constant as

$$\mu_{eff} = \sqrt{\frac{3k_B \cdot C}{N_A}}, \quad (2)$$

where N_A is the Avogadro constant and k_B is the Boltzmann constant.

The theoretical magnetic moments were calculated assuming (i) the $Sr_2Nb_1Fe_{0.6}O_{5.4}$ structure and (ii) the spin values $S = 5/2$ of magnetic ions Fe^{3+} as

$$\mu_{eff}^{Theor} = g \cdot \sqrt{N \cdot S(S+1)} \cdot \mu_B, \quad (3)$$

where $N = 0.6$ and μ_B is the Bohr magneton.

The theoretically calculated and experimentally estimated values of the effective magnetic moment almost coincide and are given in Table 1.

The negative sign of the Curie–Weiss temperature indicates the antiferromagnetic nature of exchange interactions between the spins of iron ions. The values of magnetic susceptibility obtained by us are consistent with the data from the [7] where Sr_2FeNbO_6 shows a Curie–Weiss behavior with $\mu_{eff} = 3.86\mu_B$ and $\Theta_{CW} = -58.1$ K in the temperature range between 150 and 300 K.

It should be noted that the magnetic susceptibility exhibits a wide maximum in the 14–25 K range, which is typical for low-dimensional magnetic systems. The nature of magnetic ordering can be judged from the behavior of AC magnetization. The real part of AC magnetization features a wide peak in the temperatures range of 14–25 K, which coincides with the temperature at which the local maxima of DC magnetization are observed (Fig. 3). However, there are no features in the imaginary part of the AC magnetization. According to [13], such behavior indicates the antiferromagnetic nature of magnetic orderings at these temperatures.

The magnetization isotherms are shown in Fig. 4. Small hysteresis loops at field values of ±0.1 T were observed at 300 K, most likely due to sample impurities (Fig. 4). The coercive force increases when the temperature drops below 50 K and reaches values of 30 mT and 60 mT at 10 K and 5 K, respectively. It can be assumed that the antiferromagnetic canted low-dimensional spin systems are formed in the Sr_2FeNbO_6 compound.

The electron paramagnetic resonance method makes it possible to study the behavior of low-dimensional spin systems, antiferromagnetic correlations, and phase separation in a sample [14,15]. We have analyzed the temperature dependence of the EPR spectra in Sr_2FeNbO_6

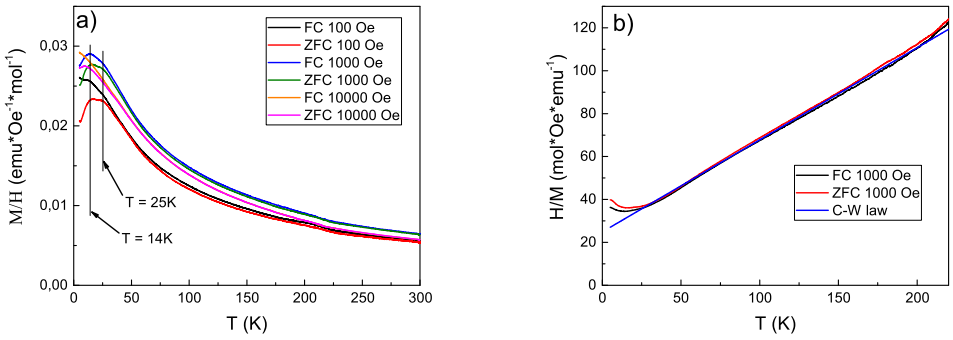

Fig. 2. Temperature dependencies of (a) DC magnetization and (b) inverse DC magnetization of Sr_2FeNbO_6. Panel (b) also shows the best fit by the Curie–Weiss law.

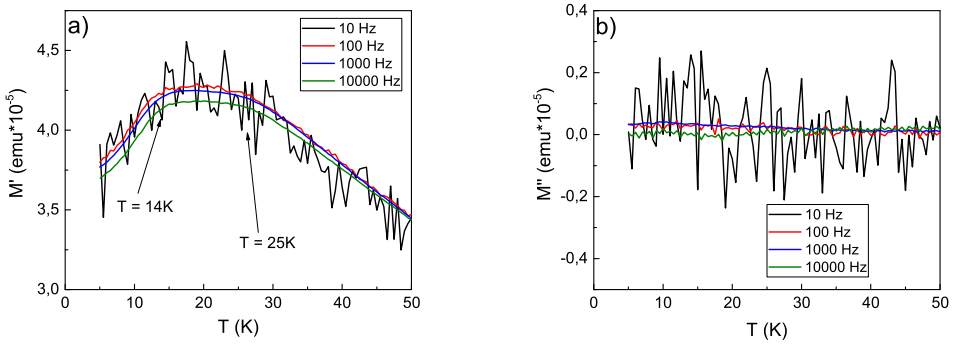

Fig. 3. Temperature dependencies of the (a) real and (b) imaginary parts of the AC magnetization of Sr_2FeNbO_6.

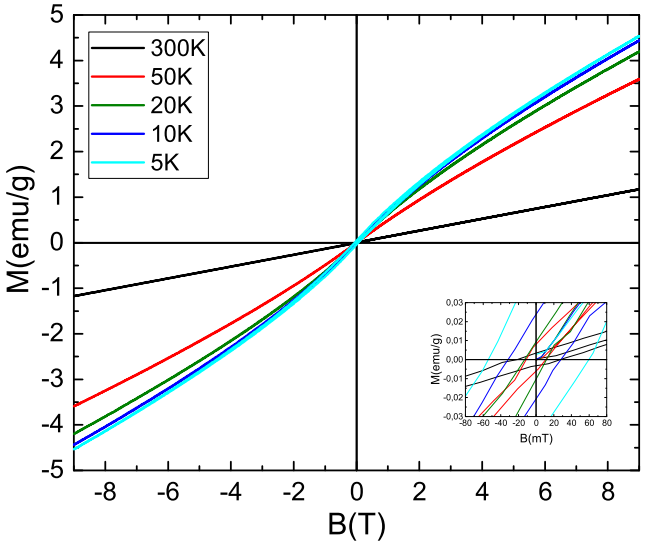

Fig. 4. Isotherms of magnetization of Sr_2FeNbO_6 at 5, 10, 20, 50, and 300 K.

in X- and Q-bands. To fit the ESR spectra between 125 K and 340 K, we used a single Lorentz line. To describe the shape of the ESR spectra below 125 K, it was necessary to consider two Lorentz lines. We can clearly see the division of ESR spectra into two EPR line for data obtained below 40 K in the Q-band. The observation of two EPR signals indicates a phase separation in the sample. If there were no phase separation, due to the exchange narrowing, only one EPR line was observed in the sample. The ESR line profile was determined by the expression:

$$\frac{dP}{dH} = \frac{d}{dH}\left(\frac{\Delta H + \alpha(H - H_{res})}{(H - H_{res})^2 + \Delta H^2} + \frac{\Delta H - \alpha(H - H_{res})}{(H + H_{res})^2 + \Delta H^2}\right), \quad (4)$$

where H_{res} is the resonance-line position, ΔH is the linewidth and α is the asymmetry parameter, which is equal to zero for Sr_2FeNbO_6. An example of the spectra decomposition into two lines is shown in Fig. 5a for X band, and spectra in Q-band are shown in Fig. 5b. As we can see in Fig. 5b the ESR line splits on two, which shifts into low magnetic fields. We include third ESR line with a very low intensity and a huge linewidth (17,000 Oe) in order to describe lineshape in the Q-band spectrum at low temperatures. The existence of this kind of line is linked to areas inside the sample where antiferromagnetic correlations have a significant impact on the linewidth. These fluctuates depend on the microwave band, and are smaller for the X-band than for the Q-band. The temperature dependencies of the linewidth, intensity, and effective g-value of two ESR lines are shown in Fig. 6. In Fig. 6, the parameters of the first and second EPR lines are shown by blue and green symbols, respectively. It should be noted that the linewidth and effective g-factor of the two ESR lines coincided for the X- and Q- data. The main difference is due to the sharp increase in the linewidth of the blue line in the X-band. We attribute this to the overlap of two ESR lines (one of which corresponds to the third ESR line of the Q-band), and the inability to separate them in the X-band with such a large linewidth and low intensity.

Let us now consider the effect of fluctuations on the temperature dependencies of the ESR linewidth near the magnetic phase transition temperature. As can be seen from Fig. 6a,d, the linewidths of the first and second EPR lines increase with decreasing temperature. We assume that the ΔH-factor shift is due not to the components of the static magnetization but to the fluctuating part of the magnetization. The maximum of the temperature dependencies of the ESR linewidth are observed at 14 K for the blue line, and at 29 K and 10 K for the green line. As the temperature decreases, the ESR linewidths are increasing due to the influence of antiferromagnetic spin correlations. The theory of critical broadening of the ESR line was developed in the works of Huber, Mori, and Kawasaki [16,17] and was first successfully used to explain the behavior of $\Delta H(T)$ in antiferromagnets in the vicinity of the Néel temperature. The temperature dependencies of both ESR

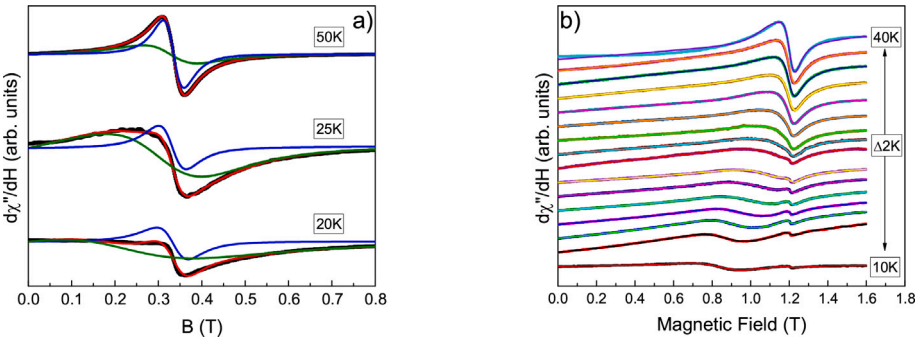

Fig. 5. ESR lines of Sr_2FeNbO_6: experiments and their best fits. (a) The first (blue line) and the second (green line) ESR lines used to fit the experimental data in X-band measurements. (b) Q-band measurements.

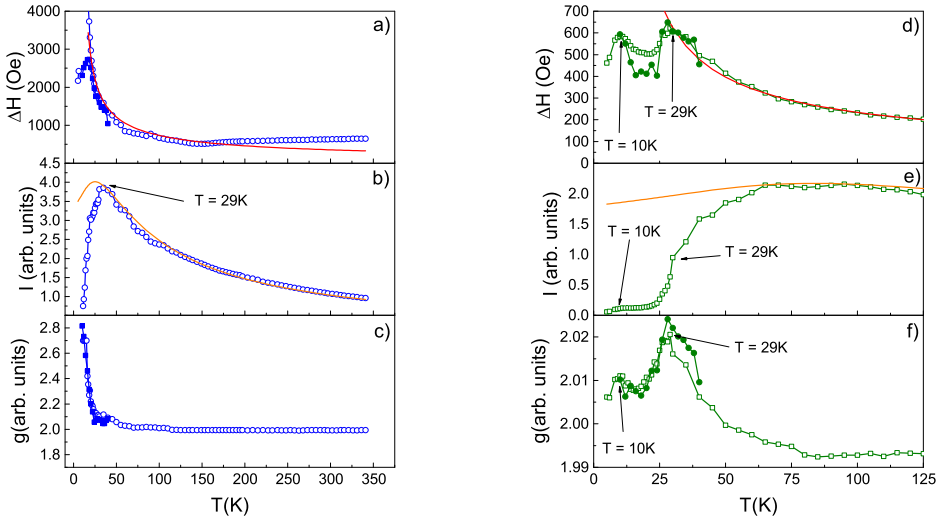

Fig. 6. (a, d) Linewidths, (b, e) Intensities, and (c, f) g-factor values of the (a–c) first and (d–f) second ESR lines of Sr_2FeNbO_6. Open symbols refer to X-band data, and solid symbols refer to Q-band data.

linewidths ΔH were fitted near antiferromagnetic ordering [14] as

$$\Delta H = \Delta H_0 + A \cdot \left[\frac{T_N}{(T - T_N)}\right]^{\beta}, \quad (5)$$

where ΔH_0 is the residual width, A is the prefactor, T_N is the transition temperature, and β is the critical exponent [15]. The fits are shown in Fig. 6a,d and the corresponding fitting parameters are given in Table 2.

The maximum temperature $T_N \approx 10$ K is in good agreement with the magnetic ordering temperature provided by the AC magnetization data. Thus, the value of $\beta = 2/3$ obtained for Sr_2FeNb_6 is close to the value for low-dimensional antiferromagnet [14].

Let us now consider the effect of fluctuations on the temperature dependencies of the ESR intensity. The intensity of the blue ESR line exhibits peaks at $T = 29$ K. The integral intensity of the green line passes through a wide maximum.

To quantify the temperature dependence of the integral intensity of the EPR line, we used the model of a quasi-one-dimensional chain of Fe^{3+} with spin $S = 5/2$. The intensities were approximated via the Bonner–Fisher formula [18]:

$$I = K \cdot \frac{C}{T \cdot (\frac{1+U}{1-U})} \quad (6)$$

$$U = coth(q) - \frac{1}{q} \quad (7)$$

$$q = \frac{2JS(S+1)}{k_B T} \quad (8)$$

The results are shown by orange lines in Fig. 6b,e and the fitting parameters are given in Table 2.

Table 2
The fitting parameters of ESR lines of Sr_2FeNbO_6.

ESR line	ΔH_0 (Oe)	A (Oe)	T_N (K)	β	J/k_B (K)
Line 1 (blue)	10	3177	9	0.64	3
Line 2 (green)		978	10	0.67	10

As can be seen from Fig. 6b,e, the integral intensity can be well approximated by the model of a quasi-one-dimensional two chain with $J_1 \approx 3$ K and $J_2 \approx 10$ K.

Now, we compare the values of the exchange integrals with the estimate provided by the Curie–Weiss temperature. The superexchange interaction integral J was estimated in the mean-field approximation using the following equation [15]:

$$\Theta_{CW} = \frac{S(S+1)}{3k_B} \sum J_i, \quad (9)$$

where J_i are isotropic exchange interactions. Substituting the absolute value of the Curie–Weiss temperature, $|\Theta_{CW}| = 60$ K, we obtained ~10 K for the value of the exchange integral, which is consistent with the values provided by the temperature dependence of the integral intensity of the EPR line. Below the ordering temperature, the integral intensities of the magnetic resonance lines decrease sharply since most of the spins have passed into an ordered state. However, we observe EPR lines below the ordering temperature that are associated with the spins of ions at the ends of antiferromagnetic chains or are located near defects. We can assume that the formation of two spin systems is due to different fillings of iron and lithium ions in the chains in the structure. One chain is filled only with iron ions, and the second includes alternating niobium and iron ions that are separated from each other by chains of non-magnetic niobium.

Let us now consider the temperature dependence of the effective g-factor shown in Fig. 6c, f. The effective g-factor is almost independent of the temperature in the 50–350 K range for the blue EPR line and is equal to 1.994 which is typical for iron ions in an octahedral environment. When the temperature drops below 50 K, the effective g-factor increases. The effective g-factor of the green line at 100 K is equal to 1.992, and the value of g_{eff} increases with decreasing temperature, featuring two maxima at 10 K and 29 K. A wide peak in the temperature range from 14 K to 29 K is also observed in AC and DC magnetization.

4. Conclusions

We synthesized double perovskite $Sr_2Fe_{0.6}NbO_{5.4}$ by pyrolysis method and obtained the Curie–Weiss temperature $\Theta_{CW} = -60$ K via fitting the temperature dependence of the inverse susceptibility by the Curie–Weiss law. The exchange integrals calculated from the temperature dependence of the integral intensity and the Curie–Weiss temperature coincide and are equal to $J/k_B \approx 10$ K. The negative sign of the Curie–Weiss temperature indicates the antiferromagnetic nature of exchange interactions between the iron spins. The phase separation is confirmed by the observation of two EPR lines in ceramics. The observation of peaks in the real part of AC magnetization, the absence of peaks in the imaginary part, and the smallness of the coercive forces in hysteresis loops confirm the canted antiferromagnetic ordering to quasi-one-dimensional states in two subsystems at ~29 K and ~14 K.

CRediT authorship contribution statement

D.V. Popov: Visualization, Writing – original draft, Writing – review & editing. **R.G. Batulin:** Investigation, Methodology. **M.A. Cherosov:** Data curation, Investigation. **I.V. Yatsyk:** Data curation, Formal analysis, Investigation, Methodology. **T.I. Chupakhina:** Investigation, Methodology, Resources. **Yu.A. Deeva:** Investigation, Resources. **R.M. Eremina:** Conceptualization, Data curation, Funding acquisition, Methodology, Project administration, Supervision, Validation, Writing – review & editing. **T. Maiti:** Conceptualization, Funding acquisition, Project administration.

Declaration of competing interest

The authors declare the following financial interests/personal relationships which may be considered as potential competing interests: Eremina R.M. reports financial support was provided by Russian Scientific Foundation.

Data availability

Data will be made available on request.

Acknowledgments

This research was supported by the Russian Science Foundation (Project No. 22-42-02014) and DST Project number DST/INT/RUS/RSF/P-55/2021. We are grateful to R.B. Zaripov for the opportunity to measure Q-band ESR data.

References

[1] P.H. Borse, C.R. Cho, S.M. Yu, J.H. Yoon, T.E. Hong, J.S. Bae, H.G. Kim, Bull. Korean Chem. Soc. 33 (10) (2012) 3407–3412.
[2] A.A. Selyutin, A.Y. Shirkin, I.A. Kasatkin, N.P. Bobrysheva, Russ. J. Gen. Chem. 85 (2015) 756–757.
[3] J.L. Rosas, J.M. Cervantes, J. León-Flores, E. Carvajal, J.A. Arenas, M. Romero, R. Escamilla, Mater. Today Commun. 23 (2020) 100844.
[4] Tao, J. Canales-Vázquez, J.T. Irvine, Chem. Mater. 16 (11) (2004) 2309–2316.
[5] R. Rodriguez, A. Fernandez, A. Isalgue, J. Rodriguez, A. Labrata, J. Tejada, X. Obradors, J. Phys. C: Solid State Phys. 18 (14) (1985) L401.
[6] M.W. Lufaso, R.B. Macquart, Y. Lee, T. Vogt, H.C. Zur Loye, J. Phys.: Condens. Matter 18 (39) (2006) 8761.
[7] N. Kashima, K. Inoue, T. Wada, Y. Yamaguchi, Appl. Phys. A 74 (2002) s805–s807.
[8] N. Rama, J.B. Philipp, M. Opel, K. Chandrasekaran, V. Sankaranarayanan, R. Gross, M.S. Rao, J. Appl. Phys. 95 (11) (2004) 7528–7530.
[9] T. Takeda, Y. Yamaguchi, H. Watanabe, J. Phys. Soc. Japan 33 (4) (1972) 967–969.
[10] H. Okuma, Y. Katayama, K. Ueno, 2022. arXiv preprint arXiv. 2209, p. 09730.
[11] D. Popov, R. Batulin, M. Cherosov, F. Vagizov, A. Zinnatullin, T. Chupakhina, Y. Deeva, T. Maiti, R. Eremina, Magnetochemistry 9 (10) (2023) 219.
[12] G.A. Bain, J.F. Berry, J. Chem. Educ. 85 (4) (2008) 532.
[13] M. Balanda, AC susceptibility studies of phase transitions and magnetic relaxation: Conventional, molecular and low-dimensional magnets, Acta Phys. Polonica A 124 (6) (2013) 964–976.
[14] A.I. Kurbakov, A.E. Susloparova, V.Y. Pomjakushin, Y. Skourski, E.L. Vavilova, T.M. Vasilchikova, G.V. Raganyan, A.N. Vasiliev, Phys. Rev. B 105 (2022) 064416.
[15] I. Yatsyk, R. Eremina, T. Chupakhina, Yu. Deeva, Magn. Reson. Solids 21 (2022) 22202.
[16] H. Mori, K. Kawasaki, Progr. Theoret. Phys. 28 (1962) 971–987.
[17] D.L. Huber, Phys. Rev. B 6 (1972) 3180.
[18] C. Venkatesh, B. Bandyopadhyay, A. Midya, K. Mahalingam, V. Ganesan, P. Mandal, Phys. Rev. B 101 (18) (2020) 184429.